NANO LETTERS

pubs.acs.org/NanoLett

Letter

Single-Atom-Based Heterojunction Coupling with Ion-Exchange Reaction for Sensitive Photoelectrochemical Immunoassay

Ying Qin, Jing Wen, Lirong Zheng, Hongye Yan, Lei Jiao, Xiaosi Wang, Xiaoli Cai, Yu Wu, Guojuan Chen, Lijuan Chen, Liuyong Hu,* Wenling Gu,* and Chengzhou Zhu*

Cite This: *Nano Lett.* 2021, 21, 1879−1887

Read Online

ACCESS | Metrics & More | Article Recommendations | Supporting Information

ABSTRACT: Benefiting from the maximum atom-utilization efficiency and distinct structural features, single-atom catalysts open a new avenue for the design of more functional catalysts, whereas their bioapplications are still in their infancy. Due to the advantages, platinum single atoms supported by cadmium sulfide nanorods (Pt SAs-CdS) are synthesized to build an ultrasensitive photoelectrochemical (PEC) biosensing platform. With the decoration of Pt SAs, the PEC signal of CdS is significantly boosted. Furthermore, theory calculations indicate the positively charged Pt SAs could change the charge distribution and increase the excited carrier density of CdS. Meanwhile, it also suggests that Cu^{2+} can severely hinder the photoexcitation and electron−hole separation of CdS. As a proof of concept, prostate-specific antigen is chosen as the target analyte to demonstrate the superiority of the Pt SAs-CdS-based PEC sensing system. As a result, the PEC biosensor based on Pt SAs-CdS exhibits outstanding detection sensitivity and promising applicability.

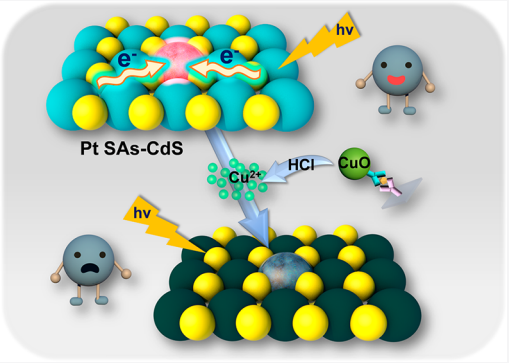

KEYWORDS: *photoelectrochemical sensors, single atoms, cadmium sulfide, photoanode, enzyme-linked immunosorbent assay*

INTRODUCTION

Single-atom catalysts (SACs), featured with isolated metal atoms on the support, have created a real sensation in the entire area of heterogeneous catalysis due to their unique electronic structures, maximum atom-utilization efficiency, and remarkable catalytic activity.[1−4] Different from the structural complexity of metal nanoparticles, the specific structures of single atoms are expected as ideal prototypes to reveal the correlations between structure and performance at the atomic scale.[5−7] To date, SACs have demonstrated extraordinary power for electrocatalysis[8,9] and photocatalysis,[10−12] such as oxygen reduction,[13] water splitting,[14] and CO_2 reduction reactions.[15] Despite the giant leaps of SACs in energy-related fields, their development in bioapplications is still at the early stage.[16,17] Hence, developing biosensors with well-designed single-atom-involved materials is of great significance.

The photoelectrochemical (PEC) biosensor, as a newly popular sensing technique, has been recognized as an elegant method for sensing trace analytes.[18−23] In a PEC sensing platform, the photoinduced current is employed as the detection signal, which plays a decisive role in highly sensitive detection.[24−31] Currently, the deposition of noble metal nanoparticles on the surface of semiconductors has been widely used in many PEC sensing systems due to the significant enhancement in photocurrent by their intrinsic plasmonic effect.[32−35] Moreover, when the contact between metal and semiconductor happens, a distinct Schottky junction can be established to promote the transfer and separation of the photogenerated electrons.[36−40] Note that the ultimate small size limit of the metal nanoparticle is a single atom, which can be stabilized by the neighboring surface atoms on the support.[41,42] Using single atoms as alternatives to nanoparticles, such nanostructured photoactive materials not only reduce the noble metal dosage but also display distinct properties. The single-atom-based photoactive material can fully inherit the fast charge carrier separation ability in a metal nanoparticle−semiconductor junction.[43,44] On the other hand, the introduction of single atoms into the framework of the semiconductors can effectively modulate the energy band and electronic structures to improve their corresponding light-harvesting and charge transport behaviors.[45−47] Meanwhile, the interfacial redox reactions can also be remarkably accelerated by single atoms due to the high catalytic activities of their unique coordination configurations.[48,49] The promoted interfacial redox reactions can reduce the aggregation of charge carriers and depress the corresponding recombination at the interface between the semiconductor and electrolyte, which

Received: January 7, 2021
Revised: February 2, 2021
Published: February 5, 2021

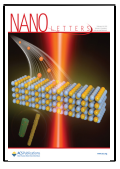

https://dx.doi.org/10.1021/acs.nanolett.1c00076
Nano Lett. 2021, 21, 1879−1887

will greatly enhance the PEC performance, as well. Therefore, developing single-atom-based photoactive materials will provide a great opportunity to build highly sensitive PEC sensing platforms.

Herein, the Pt SAs-CdS is prepared to develop a novel enzyme-free PEC immunoassay with the atomic-level heterostructure. Notably, the Pt SAs-CdS displays superior ability for the transfer of photogenerated electrons and the separation of electron−hole pairs, resulting in a significant boost of the PEC signal. According to density functional theory (DFT) calculations, the photoinduced electrons of Pt SAs-CdS could be easily excited and then transfer to Pt centers because of their higher occupation near the Fermi level and changed orbital distribution. As a proof-of-concept application, sensitive detection of prostate-specific antigen (PSA) is achieved with the Pt SAs-CdS-based PEC biosensor using CuO nanoparticles (NPs) as a mediator (Scheme 1). Upon addition of PSA, Cu^{2+} ions would be released and react with the photoelectrode materials, triggering a recession in the photocurrent signals. Finally, the PEC biosensor based on Pt SAs-CdS displays an applicative linear range and a low detection limit, holding promising applicability in practical samples for the detection of PSA. It is expected that this work can not only further expand the application scope of single-atom-involved materials but also provide guidelines for designing high-performance PEC biosensors.

Scheme 1. Schematic Illustration for the Mechanism of Pt SAs-CdS-Based PEC Biosensing Platform

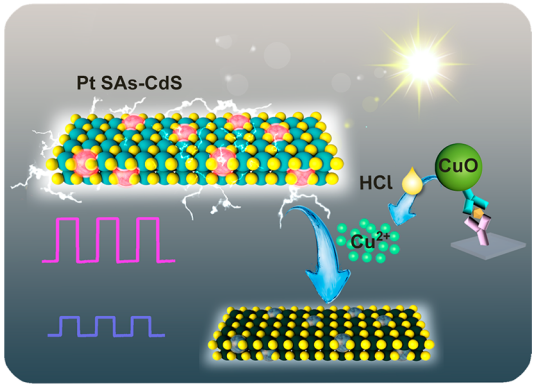

RESULTS AND DISCUSSION

The synthetic procedures of Pt SAs-CdS are displayed in Figure 1a. First, the CdS was synthesized by a facile one-pot solvothermal seeded-growth procedure. Afterward, Pt SAs-CdS was successfully obtained using CdS as the support to stabilize Pt SAs. The following heat treatment was adopted to enhance the interaction between unsaturated sulfur atoms and the isolated Pt atoms of CdS. The morphology of the as-prepared samples was characterized using scanning electron microscopy (SEM) and transmission electron microscopy (TEM). As displayed in Figure 1b, Pt SAs-CdS possesses a rod-like structure with regular diameters ranging from 53.9 to 66.6 nm, which is similar to that of CdS and Pt NPs-CdS (Figures S1 and S2). According to the elemental mapping images, the well-distributed elements of Cd, S, and Pt are observed for Pt SAs-CdS (Figure 1c). This result is in accordance with the energy-dispersive spectroscopy (EDS) spectrum of Pt SAs-CdS in Figure S3a. The high-angle annular dark-field scanning transmission electron microscope (HAADF-STEM) image (Figure S3b) shows the clear lattice fringes of 3.34 Å, which correspond to (002) planes of CdS. Meanwhile, white bright dots in the corresponding aberration-corrected HAADF-STEM (AC-HAADF-STEM) image (Figure 1d) reveal the atomically dispersed Pt. Furthermore, the crystal structure of the samples was characterized by X-ray diffraction (XRD). In Figure S4, Pt SAs-CdS exhibits the characteristic diffraction peaks of standard CdS (JCPDS 77-2306), and no other diffraction peaks are found, revealing the absence of Pt-based crystalline phases. In addition, the local atomic coordination and electronic structure of Pt were further studied with X-ray absorption spectroscopy (XAS). As shown in the X-ray absorption near-edge structure (XANES) analysis of the Pt L_3-edge, the absorption edge position of Pt SAs-CdS is located between those of the Pt foil and PtO_2, suggesting that the Pt single atoms are positively charged (Figure 1e). On the basis of extended X-ray absorption fine structure (EXAFS) analysis in Figure 1f, Pt SAs-CdS exhibits a prominent peak at about 1.76 Å, which is associated with Pt−S scattering. Notably, the signal from the Pt−Pt contribution (2.6 Å) is not observed, demonstrating the single-atom Pt sites in Pt SAs-CdS. For comparison, the sample of Pt NPs-CdS was also prepared by anchoring Pt NPs on the surface of the CdS. As depicted in Figure S2b, the existence of Pt NPs could be confirmed.

To confirm the effect of Pt single atoms on the properties of photoactive material, the PEC and spectroscopic tests were systematically performed. The electronic structures of Pt SAs-CdS, Pt NPs-CdS, and CdS were carefully analyzed by X-ray photoelectron spectroscopy (XPS) measurements. As a result, the binding energies of S 2p and Cd 3d in Pt SAs-CdS positively shifted by 0.4 and 0.6 eV, respectively, relative to those of CdS, indicating the electron depletion after introducing Pt SAs (Figure 2a and Figure S6a). The strong electronic coupling between Pt SAs and CdS suggests the formation of an effective heterojunction, which favors the PEC performance. Moreover, the deconvoluted peak at 163.04 eV is observed with Pt SAs-CdS, which could be ascribed to the signal of newly generated Pt−S coordinated bonds.[50] Meanwhile, electron paramagnetic resonance (EPR) spectroscopy was employed to elucidate the photoinduced electron injection process, as well (Figure S7). After irradiation for 10 min, the sample of Pt SAs-CdS shows one single Lorentzian line centered at 322.4 mT (g = 2.105).[51] Compared with the bare CdS, a stronger EPR signal of Pt SAs-CdS indicates a higher concentration of unpaired electrons, which can facilitate separation efficiency of the photoinduced electron−hole pairs.[52] Generally speaking, the steady-state photoluminescence (PL) phenomenon is closely related to the recombination of photogenerated electrons and holes in a semiconductor. A strong PL signal of the semiconductor means serious radiative recombination, leading to a poor PEC performance. As described in Figure 2b, the sample of Pt SAs-CdS exhibits a strongly quenched PL intensity compared with the pristine CdS, indicating the recombination of photogenerated electrons and holes is largely suppressed by the decorated Pt SAs. Moreover, Pt SAs-CdS presents a conductivity better than those of CdS and Pt NPs-CdS due to the smaller charge transfer resistance in electrochemical impedance spectroscopy (EIS) (Figure 2c). Then, the transient photocurrent responses with consecutive on−off light irradiation were studied at 0 V (Figure 2d). As expected, the photoelectrode based on Pt SAs-CdS manifests a significant PEC response, which is nearly 1.8

https://dx.doi.org/10.1021/acs.nanolett.1c00076
Nano Lett. 2021, 21, 1879−1887

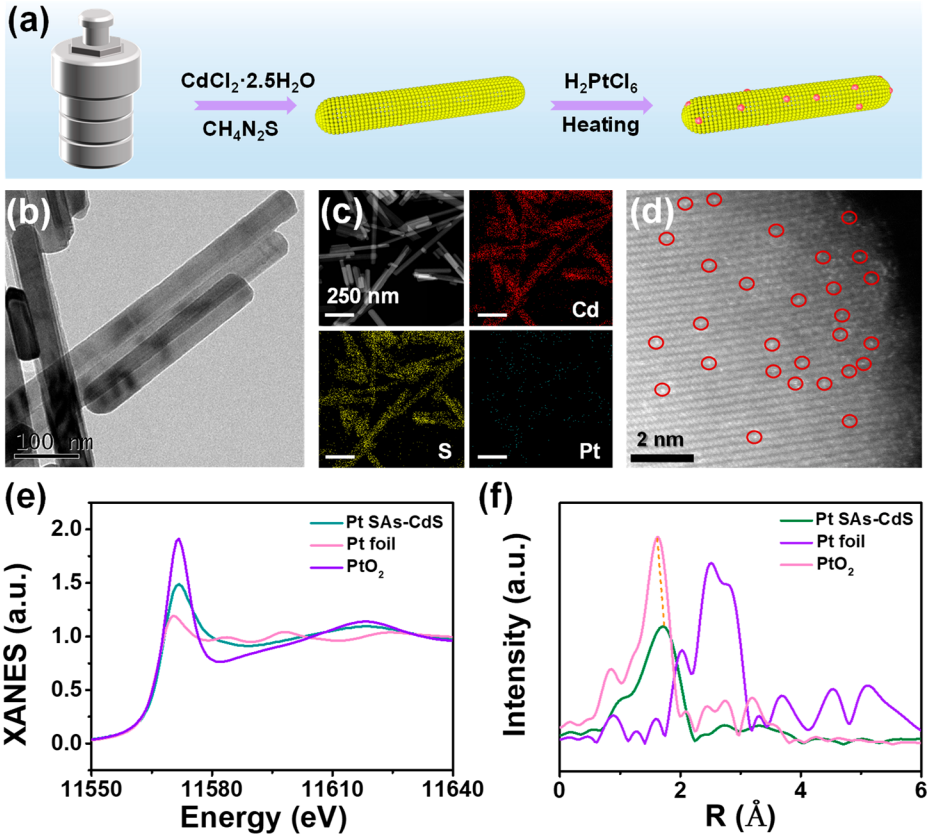

Figure 1. (a) Schematic diagram for the preparation of Pt SAs-CdS. (b) TEM, (c) EDS mapping, and (d) AC-HAADF-STEM images of Pt SAs-CdS. (e) XANES and (f) EXAFS spectra of Pt SAs-CdS, Pt foil, and PtO_2.

and 5.2 times higher than those of Pt-NP-CdS and bare CdS NRs, respectively. In addition, the photoresponse of Pt SAs-CdS and CdS was also studied by linear sweep voltammetry (LSV) tests (Figure S10), which were recorded under a bias potential range between −0.2 and 0.2 V (vs Ag/AgCl). The photocurrent of Pt SAs-CdS increases rapidly with the positive-scanning potential steps, manifesting a typical n-type semiconductor feature. The excellent PEC response could be attributed to the boosted electron−hole pair separation efficiency in the photoactive material of Pt SAs-CdS, which is in accordance with the above characterizations. To reveal the influence of Pt SAs on light absorption properties and energy structure, the UV−vis diffuse-reflectance spectra were acquired in the range of 200−800 nm (Figure S8a). CdS is observed with the typical light absorption edge of 525 nm,[53] whereas the slightly red-shifted absorption edge is realized after the introduction of Pt species, which is conducive to enhance the light-harvesting ability of photoactive material. Then, the band gap energy (E_g) of CdS is calculated as 2.36 eV according to the Tauc plot transformed from the UV−vis diffuse-reflectance spectrum of CdS (Figure S8b).[54] To obtain the band structure of CdS, the Mott−Schottky curve was measured (Figure S9) and the flat-band potential (E_{fb}) of CdS was −0.97 V vs SCE (−0.72 V vs NHE). The slope of the tangent of CdS in the Mott−Schottky spectrum is positive, also indicating its n-type characteristic. Generally, the E_{fb} is 0.1 eV more positive than the conduction band potential (E_{cb}).[55] Hence, the E_{cb} of CdS is approximately −0.82 eV vs NHE, and the valence band potential (E_{vb}) of CdS is calculated to be 1.54 eV accordingly. As a result, the energy band structure diagram is illustrated in Figure 2e, and the corresponding mechanism on Pt SAs facilitating the photoelectron transfer is proposed. During the PEC process, Na_2SO_3 acts as the hole-scavenging agent to prevent photocorrosion and improve the stability of the working electrode.

Specifically, the splendid nature of the single-atom-based photoactive material is favorable to create an ultrasensitive biosensor. Taking PSA as a representative analyte, the as-prepared Pt SAs-CdS was then tested for PEC immunoassay using CuO NPs for signal labeling. According to the UV−visible spectra, Cu_2O-Ab_2 displayed a broad peak in the range of 230−310 nm compared with that of Ab_2 (Figure S11), which may be caused by the overlay of CuO NPs and Ab_2. To further confirm the combination of CuO NPs and Ab_2, the confocal laser scanning microscopy (CLSM) analysis was adopted. As disclosed in Figure S12, a red fluorescence region in the images of CLSM for CuO-Ab_2 was observed, indicating the successful immobilization of Ab_2 on CuO. Meanwhile, the Fourier transform infrared (FT-IR) spectra also demonstrate the above result due to the appearance of vibration peaks of $-NH_2$ and −COOH in Figure S13. CuO NPs can be dissociated into Cu^{2+} ions under acidic conditions, which subsequently convert CdS into CuS_x via an ion-exchange reaction during this process, changing the properties of the Pt SAs-CdS photoelectrode.[56] To gain an in-depth understanding of the influence of Cu^{2+} ions on the properties of the Pt SAs-CdS photoelectrode, PL emission spectra of the samples with or without Cu^{2+} ions were collected. In Figure S14, a higher PL intensity is obtained in the presence of Cu^{2+} ions, implying that the addition of Cu^{2+} could induce the electron−hole recombination in Pt SAs-CdS. Moreover, the time-resolved photoluminescence (TRPL) spectra (Figure 2f) were also

https://dx.doi.org/10.1021/acs.nanolett.1c00076
Nano Lett. 2021, 21, 1879−1887

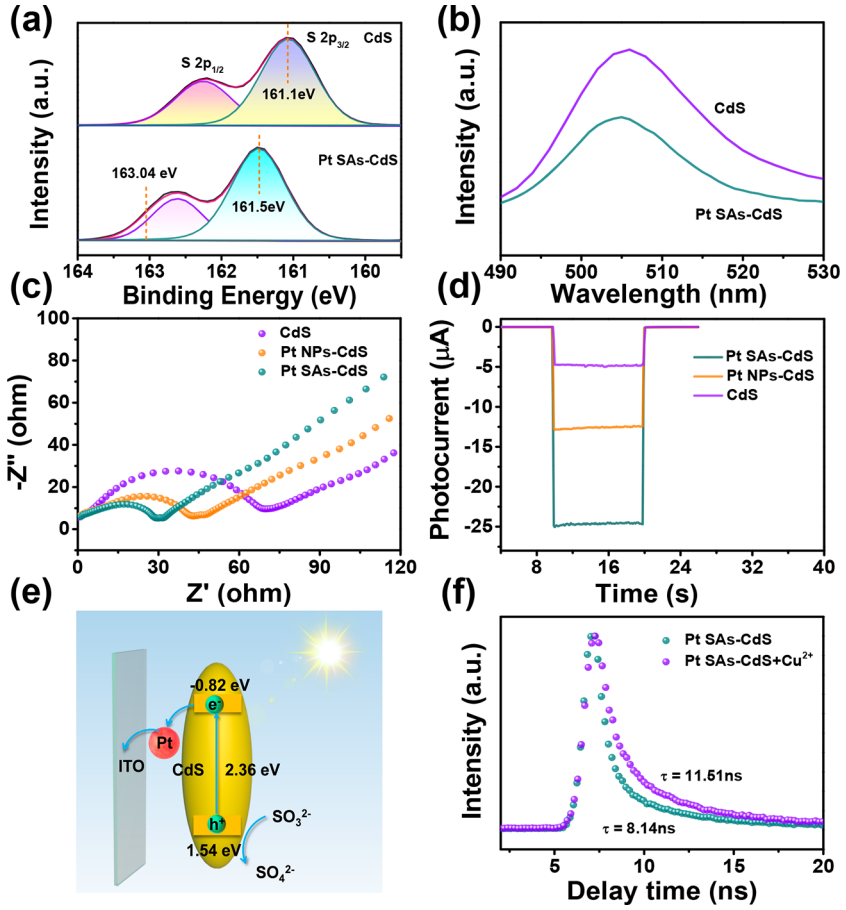

Figure 2. (a) S 2p XPS results of CdS and Pt SAs-CdS. (b) Steady-state PL spectra of CdS and Pt SAs-CdS. (c) EIS and (d) photocurrent responses for CdS, Pt SAs-CdS, and Pt NPs-CdS. (e) Schematic band structure of Pt SAs-CdS. (f) Time-resolved transient photoluminescence decay for Pt SAs-CdS and Pt SAs-CdS+Cu^{2+}.

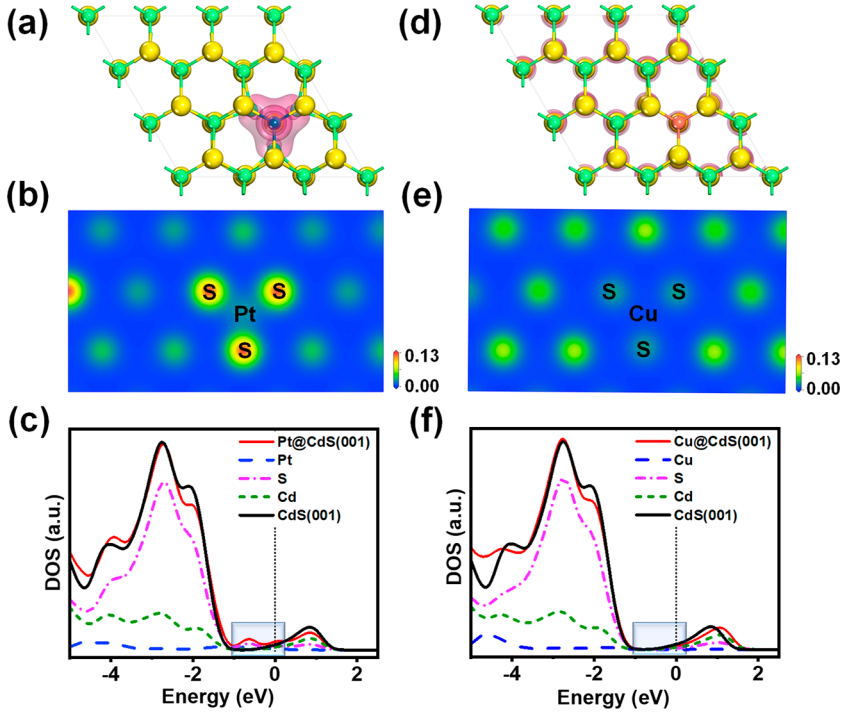

Figure 3. (a,d) Optimized structures with the lowest orbital distributions of the conduction band (S, yellow; Cd, green; Cu, orange; Pt, dark blue), (b,e) charge density distributions, and (c,f) partial density of states of Pt and Cu adatoms embedded and pure S-terminated CdS (001).

https://dx.doi.org/10.1021/acs.nanolett.1c00076
Nano Lett. 2021, 21, 1879−1887

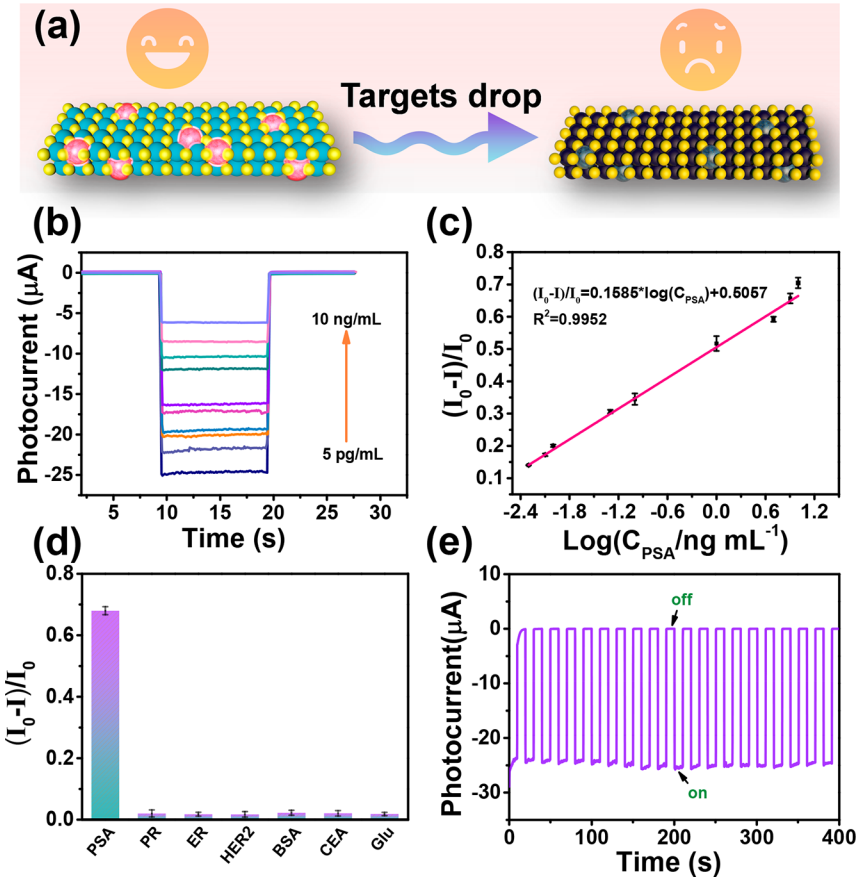

Figure 4. (a) Schematic illustration of Pt SAs-CdS-based biosensing. (b) Photocurrent responses of Pt SAs-CdS/ITO with different concentration target PSA. (c) Calibration curve. (d) Selectivity of this immunosensing platform against PSA (10 ng/mL), PR (1 mg/mL), ER (1 mg/mL), HER2 (1 mg/mL), BSA (1 mg/mL), CEA (1 mg/mL), and Glu (1 mg/mL). (e) Stability of Pt SAs-CdS/ITO.

conducted to reveal the changes in photogenerated charge transfer dynamics after introducing Cu^{2+} ions, in which all spectra were fitted with the fast ($\tau 1$, $\tau 2$) and slow ($\tau 3$) lifetime components (Table S1).[57] Similar values of $\tau 1$ (0.23−0.24 ns) and $\tau 2$ (2.30−2.39 ns) are yielded, whereas $\tau 3$ largely increases from 5.50 to 8.98 ns after adding Cu^{2+} ions. The slow decay time indicates a sluggish dynamic of photogenerated electron−hole pair separation. As a result, the average lifetime of Pt SAs-CdS is lengthened from 8.14 to 11.51 ns upon addition of Cu^{2+} ions, indicating that the commendable charge transfer channels provided by Pt SAs are destroyed after adding Cu^{2+} ions. Based on the above, the photocurrent responses of Pt SAs-CdS before and after adding Cu^{2+} ions are presented in Figure S15a, and a depressed PEC performance is observed with the presence of Cu^{2+} ions. In addition, the EIS measurement was also performed after the introduction of Cu^{2+} ions, and a larger charge transfer resistance is observed, which is in accordance with the decreased photocurrent (Figure S15b).

Furthermore, density functional theory (DFT) calculations were performed to demonstrate the geometric and electronic structures of the Pt and Cu adatom-doped CdS (001) surface, which could be helpful to understand the different electron transfer behaviors during the PEC process. Two different loading modes were studied here (Figure S16), and the most relatively stable structures are shown in Figure 3a,d, where S-terminated CdS (001) with one Cd atom near the surface was replaced with a Pt or Cu adatom. The lowest orbital distributions of the conduction band in Figure 3a,d are different, and the localized orbital on Pt−S4 bonds could be beneficial to concentrate excitons. In Figure 3b, Hirshfeld charge analysis reveals that the Pt adatom could induce a charge trapping state of S-terminated CdS (001), which is favors receiving photogenerated electrons, whereas this phenomenon is inconspicuous in the Cu-embedded structure in Figure 3e. These different orbital and electron distributions between Pt and Cu doping systems could be further revealed by their partial density of states in Figure 3c,f, and the Pt-embedded S-terminated CdS (001) structure shows higher occupation near the Fermi level (see the curves of the density of states in the transparent blue region). This result implies that the photoinduced electrons could be easily excited and transfer to the Pt active sites, leading to a remarkably enhanced PEC performance. Additionally, the conduction band of the Cu-embedded structure was positively shifted compared to that with pure CdS (001) (see Figure 3f), resulting in the decreased excitation for photogenerated electrons. Consequently, the DFT calculations support that the as-synthesized Pt SAs-CdS can realize directional migration of photoinduced exciton to the Pt−S4 area and further supply an efficient separation of electron−hole pairs. On the contrary, when the Cu^{2+} was added in Pt SAs-CdS, the separation of a photogenerated exciton could be prevented, leading to an inferior photocurrent.

To guarantee sensitive biosensing, the detection condition was carefully optimized. First, the loading content of Pt SAs at the surface of CdS was finely adjusted, and the Pt SAs-CdS

https://dx.doi.org/10.1021/acs.nanolett.1c00076
Nano Lett. 2021, 21, 1879−1887

with a feed ratio of 0.4% exhibits the largest photocurrent (Figure S17a). Afterward, the thicknesses of the photoelectrode were studied by drop-coating with different volumes of photoactive material, which is necessary for the light-harvesting and charge transport. As plotted in Figure S17b, the strongest PEC signal is achieved by a volume of 13 μL of Pt SAs-CdS, which is used for the following tests. To ensure a sufficient reaction with Cu^{2+} ions, the photocurrent of the different samples with the reaction time ranging from 5 to 35 min was measured in Figure S17c. It is found that the photocurrent signals are almost unchanged after incubation for 25 min. As schematically illustrated in Figure 4a, the single-atom-based photoactive material with the excellent PEC performance was used to build a negatively correlated biosensor. Considering the CuO NPs-labeled sandwich immunocomplexes induced PEC signal inhibition, the relationship between the PSA concentrations and photocurrent inhibition was well-developed. As a result, the photocurrent values of Pt SAs-CdS linearly decreased with the PSA concentrations from 5 pg/mL to 10 ng/mL (Figure 4b). The linear regression equation (Figure 4c) can be expressed as $(I_0 - I)/I_0 = 0.1585 \log(C_{PSA}) + 0.5057$ ($R^2 = 0.9952$), and the limit of detection is 0.92 pg/mL (signal-to-noise ratio of 3). As displayed in Table S2, different methods for the detection of PSA are also compared, and the as-prepared PEC biosensor in this work is among the best-known results.

The selectivity of the PEC immunoassay was also studied by introducing some interferences, including progesterone receptor (PR), human epidermal growth factor receptor-2 (HER2), estrogen receptor (ER), bovine serum albumin (BSA), carcinoembryonic antigen (CEA), and glucose (Glu). Even using a 100-fold higher concentration than PSA (10 ng/mL), the photocurrent suppression rates of the interferences are still ignorable, proving the excellent selectivity of the fabricated biosensor for PSA (Figure 4d). Furthermore, the developed Pt SAs-CdS photoelectrode exhibits outstanding PEC stability under a periodic on−off light for 400 s (Figure 4e). To verify the practical usability and reliability of the as-obtained PEC biosensor, the detection of PSA in human serum samples was carried out. As depicted in Table 1, the test results

Table 1. Comparison of the Pt SAs-CdS Biosensor and the Test Result from the Hospital

	serum samples (ng/mL)	biosensor (ng/mL)	relative standard deviation (%)
1	0.2952	0.3019 ± 0.01	4.090
2	0.4080	0.4065 ± 0.01	2.020
3	0.7380	0.7337 ± 0.02	2.120
4	1.930	1.948 ± 0.05	2.590

based on this PEC biosensor in human serum samples are close to the values detected by the hospital with the chemiluminescence method. The relative standard deviations are less than 4.09%, implying the feasibility of the developed biosensor for real sample tests.

CONCLUSION

In this work, an advanced PEC sensing platform was developed using Pt SAs-CdS with ultrahigh photoactivity for detecting PSA. Aberration-corrected HAADF-STEM and XANES results fully demonstrated the monatomic characteristic of as-prepared Pt SAs-CdS. As a direct result, the maximum atom utilization efficiency of the noble metals is realized by the isolated platinum centers of Pt SAs-CdS, displaying a PEC performance much higher than that of Pt NPs-CdS and CdS owing to the accelerated photogenerated charge carries separations. Finally, the Pt SAs-CdS-based PEC biosensor exhibits a good linear relationship range from 5 pg/mL to 10 ng/mL PSA with a very low detection limit of 0.92 pg/mL. In addition, the Pt SAs-CdS-based PEC sensing platform exhibits good selectivity and promising detection in human serum samples. Expectantly, the single-atom-based photoactive material opens a new avenue for designing high-performance PEC biosensors and further expands the application scope of single-atom-involved materials.

ASSOCIATED CONTENT

Supporting Information

The Supporting Information is available free of charge at https://pubs.acs.org/doi/10.1021/acs.nanolett.1c00076.

Experimental section, Figures S1−S18, and Tables S1 and S2 (PDF)

AUTHOR INFORMATION

Corresponding Authors

Liuyong Hu − *Hubei Engineering Technology Research Center of Optoelectronic and New Energy Materials, Hubei Key Laboratory of Plasma Chemistry and Advanced Materials, School of Materials Science and Engineering, Wuhan Institute of Technology, Wuhan 430205, P.R. China*; Email: huly@wit.edu.cn

Wenling Gu − *Key Laboratory of Pesticide and Chemical Biology of Ministry of Education, International Joint Research Center for Intelligent Biosensing Technology and Health, College of Chemistry, Central China Normal University, Wuhan 430079, P.R. China*; Email: wlgu@mail.ccnu.edu.cn

Chengzhou Zhu − *Key Laboratory of Pesticide and Chemical Biology of Ministry of Education, International Joint Research Center for Intelligent Biosensing Technology and Health, College of Chemistry, Central China Normal University, Wuhan 430079, P.R. China*; orcid.org/0000-0003-0679-7965; Email: czzhu@mail.ccnu.edu.cn

Authors

Ying Qin − *Key Laboratory of Pesticide and Chemical Biology of Ministry of Education, International Joint Research Center for Intelligent Biosensing Technology and Health, College of Chemistry, Central China Normal University, Wuhan 430079, P.R. China*

Jing Wen − *Hubei Engineering Technology Research Center of Optoelectronic and New Energy Materials, Hubei Key Laboratory of Plasma Chemistry and Advanced Materials, School of Materials Science and Engineering, Wuhan Institute of Technology, Wuhan 430205, P.R. China*

Lirong Zheng − *Institute of High Energy Physics, Chinese Academy of Sciences, Beijing 100049, P. R. China*

Hongye Yan − *Key Laboratory of Pesticide and Chemical Biology of Ministry of Education, International Joint Research Center for Intelligent Biosensing Technology and Health, College of Chemistry, Central China Normal University, Wuhan 430079, P.R. China*

Lei Jiao − *Key Laboratory of Pesticide and Chemical Biology of Ministry of Education, International Joint Research Center for*

https://dx.doi.org/10.1021/acs.nanolett.1c00076
Nano Lett. 2021, 21, 1879−1887

Intelligent Biosensing Technology and Health, College of Chemistry, Central China Normal University, Wuhan 430079, P.R. China

Xiaosi Wang − *Key Laboratory of Pesticide and Chemical Biology of Ministry of Education, International Joint Research Center for Intelligent Biosensing Technology and Health, College of Chemistry, Central China Normal University, Wuhan 430079, P.R. China*

Xiaoli Cai − *Key Laboratory of Pesticide and Chemical Biology of Ministry of Education, International Joint Research Center for Intelligent Biosensing Technology and Health, College of Chemistry, Central China Normal University, Wuhan 430079, P.R. China*

Yu Wu − *Key Laboratory of Pesticide and Chemical Biology of Ministry of Education, International Joint Research Center for Intelligent Biosensing Technology and Health, College of Chemistry, Central China Normal University, Wuhan 430079, P.R. China*

Guojuan Chen − *Key Laboratory of Pesticide and Chemical Biology of Ministry of Education, International Joint Research Center for Intelligent Biosensing Technology and Health, College of Chemistry, Central China Normal University, Wuhan 430079, P.R. China*

Lijuan Chen − *Department of Medical Imaging, Henan Provincial People's Hospital & the People's Hospital of Zhengzhou University, Zhengzhou 450003, P. R. China*

Complete contact information is available at: https://pubs.acs.org/10.1021/acs.nanolett.1c00076

Author Contributions

Y.Q.: investigation, data curation, writing the original draft. J.W.: theoretical calculation. L.Z.: X-ray absorption near-edge structure analysis. H.Y.: helped with enzyme-linked immunosorbent assay. L.J.: formal analysis, review and editing. X.W.: helped with ultraviolet−visible diffuse-reflectance absorption. X.C.: helped with confocal laser scanning microscopy. Y.W.: table of contents analysis, review and editing. G.C.: validation. L.C.: provided real samples. L.H.: supervision, conceptualization, writing, review, and editing. W.G.: supervision, methodology, formal analysis. C.Z.: supervision, funding acquisition, writing, review, and editing, project administration. Y.Q. and J.W. contributed equally to this work.

Notes

The authors declare no competing financial interest.

■ ACKNOWLEDGMENTS

This work was supported by National Natural Science Foundation of China (Nos. 22074049 and 22004042), Natural Science Foundation of Hubei Province (2020CFB276), self-determined research funds of CCNU from the colleges' basic research and operation of MOE (CCNU20QN007 and CCNU20TS013), and the Program of Introducing Talents of Discipline to Universities of China (111 program, B17019). We thank the 1W1B station in Beijing Synchrotron Radiation Facility (BSRF) for X-ray absorption spectroscopy measurements.

■ REFERENCES

(1) Qiao, B.; Wang, A.; Yang, X.; Allard, L. F.; Jiang, Z.; Cui, Y.; Liu, J.; Li, J.; Zhang, T. Single-Atom Catalysis of CO Oxidation Using Pt_1/FeO_x. *Nat. Chem.* **2011**, *3*, 634−641.

(2) Yang, X.-F.; Wang, A.; Qiao, B.; Li, J.; Liu, J.; Zhang, T. Single-Atom Catalysts: A New Frontier in Heterogeneous Catalysis. *Acc. Chem. Res.* **2013**, *46*, 1740−1748.

(3) Jiao, L.; Wu, J.; Zhong, H.; Zhang, Y.; Xu, W.; Wu, Y.; Chen, Y.; Yan, H.; Zhang, Q.; Gu, W.; Gu, L.; Beckman, S. P.; Huang, L.; Zhu, C. Densely Isolated FeN_4 Sites for Peroxidase Mimicking. *ACS Catal.* **2020**, *10*, 6422−6429.

(4) Gu, W.; Wang, H.; Jiao, L.; Wu, Y.; Chen, Y.; Hu, L.; Gong, J.; Du, D.; Zhu, C. Single-Atom Iron Boosts Electrochemiluminescence. *Angew. Chem., Int. Ed.* **2020**, *59*, 3534−3538.

(5) Lai, W.; Miao, Z.; Wang, Y.; Wang, J.; Chou, S. Atomic-Local Environments of Single-Atom Catalysts: Synthesis, Electronic Structure, and Activity. *Adv. Energy Mater.* **2019**, *9*, 1900722.

(6) Jeong, H.; Shin, D.; Kim, B. S.; Bae, J.; Shin, S.; Choe, C.; Han, J. W.; Lee, H. Controlling the Oxidation State of Pt Single Atoms for Maximizing Catalytic Activity. *Angew. Chem., Int. Ed.* **2020**, *59*, 20691−20696.

(7) Li, Z.; Ji, S.; Liu, Y.; Cao, X.; Tian, S.; Chen, Y.; Niu, Z.; Li, Y. Well-Defined Materials for Heterogeneous Catalysis: From Nanoparticles to Isolated Single-Atom Sites. *Chem. Rev.* **2020**, *120*, 623−682.

(8) Zhu, C.; Fu, S.; Shi, Q.; Du, D.; Lin, Y. Single-Atom Electrocatalysts. *Angew. Chem., Int. Ed.* **2017**, *56*, 13944−13960.

(9) Wu, J.; Xiong, L.; Zhao, B.; Liu, M.; Huang, L. Densely Populated Single Atom Catalysts. *Small Methods* **2020**, *4*, 1900540.

(10) Li, X.; Bi, W.; Zhang, L.; Tao, S.; Chu, W.; Zhang, Q.; Luo, Y.; Wu, C.; Xie, Y. Single-Atom Pt as Co-Catalyst for Enhanced Photocatalytic H_2 Evolution. *Adv. Mater.* **2016**, *28*, 2427−2431.

(11) Wang, Q.; Zhang, D.; Chen, Y.; Fu, W.; Lv, X. J. Single-Atom Catalysts for Photocatalytic Reactions. *ACS Sustainable Chem. Eng.* **2019**, *7*, 6430−6443.

(12) Li, Q.; Chen, W.; Xiao, H.; Gong, Y.; Li, Z.; Zheng, L.; Zheng, X.; Yan, W.; Cheong, W. C.; Shen, R.; Fu, N.; Gu, L.; Zhuang, Z.; Chen, C.; Wang, D.; Peng, Q.; Li, J.; Li, Y. Fe Isolated Single Atoms on S, N Codoped Carbon by Copolymer Pyrolysis Strategy for Highly Efficient Oxygen Reduction Reaction. *Adv. Mater.* **2018**, *30*, 1800588.

(13) Luo, X.; Wei, X.; Wang, H.; Gu, W.; Kaneko, T.; Yoshida, Y.; Zhao, X.; Zhu, C. Secondary-Atom-Doping Enables Robust Fe-N-C Single-Atom Catalysts with Enhanced Oxygen Reduction Reaction. *Nano-Micro Lett.* **2020**, *12*, 163.

(14) Ling, C.; Shi, L.; Ouyang, Y.; Zeng, X. C.; Wang, J. Nanosheet Supported Single-Metal Atom Bifunctional Catalyst for Overall Water Splitting. *Nano Lett.* **2017**, *17*, 5133−5139.

(15) Pan, Y.; Lin, R.; Chen, Y.; Liu, S.; Zhu, W.; Cao, X.; Chen, W.; Wu, K.; Cheong, W. C.; Wang, Y.; Zheng, L.; Luo, J.; Lin, Y.; Liu, Y.; Liu, C.; Li, J.; Lu, Q.; Chen, X.; Wang, D.; Peng, Q.; Chen, C.; Li, Y. Design of Single-Atom Co-N_5 Catalytic Site: A Robust Electrocatalyst for CO_2 Reduction with Nearly 100% CO Selectivity and Remarkable Stability. *J. Am. Chem. Soc.* **2018**, *140*, 4218−4221.

(16) Wu, Y.; Wu, J.; Jiao, L.; Xu, W.; Wang, H.; Wei, X.; Gu, W.; Ren, G.; Zhang, N.; Zhang, Q.; Huang, L.; Gu, L.; Zhu, C. Cascade Reaction System Integrating Single-Atom Nanozymes with Abundant Cu Sites for Enhanced Biosensing. *Anal. Chem.* **2020**, *92*, 3373−3379.

(17) Jiao, L.; Xu, W.; Wu, Y.; Yan, H.; Gu, W.; Du, D.; Lin, Y.; Zhu, C. Single-Atom Catalysts Boost Signal Amplification for Biosensing. *Chem. Soc. Rev.* **2021**, *50*, 750.

(18) Li, Y.; Ma, M.; Zhu, J. Dual-Signal Amplification Strategy for Ultrasensitive Photoelectrochemical Immunosensing of α-Fetoprotein. *Anal. Chem.* **2012**, *84*, 10492−10499.

(19) Zhang, Y.; Li, M.; Wang, H.; Yuan, R.; Wei, S. Supersensitive Photoelectrochemical Aptasensor Based on Br, N-Codoped TiO_2 Sensitized by Quantum Dots. *Anal. Chem.* **2019**, *91*, 10864−10869.

(20) Shu, J.; Qiu, Z.; Lv, S.; Zhang, K.; Tang, D. Plasmonic Enhancement Coupling with Defect-Engineered TiO_{2-x}: A Mode for Sensitive Photoelectrochemical Biosensing. *Anal. Chem.* **2018**, *90*, 2425−2429.

(21) Tian, J.; Zhu, H.; Chen, J.; Zheng, X.; Duan, H.; Pu, K.; Chen, P. Cobalt Phosphide Double-Shelled Nanocages: Broadband Light-Harvesting Nanostructures for Efficient Photothermal Therapy and

Self-Powered Photoelectrochemical Biosensing. *Small* **2017**, *13*, 1700798.
(22) Xu, R.; Wei, D.; Du, B.; Cao, W.; Fan, D.; Zhang, Y.; Wei, Q.; Ju, H. A Photoelectrochemical Sensor for Highly Sensitive Detection of Amyloid Beta Based on Sensitization of Mn:CdSe to Bi_2WO_6/CdS. *Biosens. Bioelectron.* **2018**, *122*, 37−42.
(23) Bellani, S.; Ghadirzadeh, A.; Meda, L.; Savoini, A.; Tacca, A.; Marra, G.; Meira, R.; Morgado, J.; Di Fonzo, F.; Antognazza, M. R. Hybrid Organic/Inorganic Nanostructures for Highly Sensitive Photoelectrochemical Detection of Dissolved Oxygen in Aqueous Media. *Adv. Funct. Mater.* **2015**, *25*, 4531−4538.
(24) Long, Y.; Kong, C.; Li, D.; Li, Y.; Chowdhury, S.; Tian, H. Ultrasensitive Determination of Cysteine Based on the Photocurrent of Nafion-Functionalized CdS-MV Quantum Dots on an ITO Electrode. *Small* **2011**, *7*, 1624−1628.
(25) Tang, J.; Li, J.; Zhang, Y.; Kong, B.; Yiliguma; Wang, Y.; Quan, Y.; Cheng, H.; Al-Enizi, A. M.; Gong, X.; Zheng, G. Mesoporous Fe_2O_3-CdS Heterostructures for Real-Time Photoelectrochemical Dynamic Probing of Cu^{2+}. *Anal. Chem.* **2015**, *87*, 6703−6708.
(26) Ma, W.; Han, D.; Zhou, M.; Sun, H.; Wang, L.; Dong, X.; Niu, L. Ultrathin g-C_3N_4/TiO_2 Composites as Photoelectrochemical Elements for the Real-Time Evaluation of Global Antioxidant Capacity. *Chem. Sci.* **2014**, *5*, 3946−3951.
(27) Dai, W.; Zhang, L.; Zhao, W.; Yu, X.; Xu, J.; Chen, H. Hybrid PbS Quantum Dot/Nanoporous NiO Film Nanostructure: Preparation, Characterization, and Application for a Self-Powered Cathodic Photoelectrochemical Biosensor. *Anal. Chem.* **2017**, *89*, 8070−8078.
(28) Zeng, X.; Tu, W.; Li, J.; Bao, J.; Dai, Z. Photoelectrochemical Biosensor Using Enzyme-Catalyzed in Situ Propagation of CdS Quantum Dots on Graphene Oxide. *ACS Appl. Mater. Interfaces* **2014**, *6*, 16197−16203.
(29) Tang, J.; Kong, B.; Wang, Y.; Xu, M.; Wang, Y.; Wu, H.; Zheng, G. Photoelectrochemical Detection of Glutathione by IrO_2-Hemin-TiO_2 Nanowire Arrays. *Nano Lett.* **2013**, *13*, 5350−5354.
(30) Ge, L.; Hong, Q.; Li, H.; Liu, C.; Li, F. Direct-Laser-Writing of Metal Sulfide-Graphene Nanocomposite Photoelectrode toward Sensitive Photoelectrochemical Sensing. *Adv. Funct. Mater.* **2019**, *29*, 1904000.
(31) Zeng, R.; Luo, Z.; Su, L.; Zhang, L.; Tang, D.; Niessner, R.; Knopp, D. Palindromic Molecular Beacon Based Z-Scheme BiOCl-Au-CdS Photoelectrochemical Biodetection. *Anal. Chem.* **2019**, *91*, 2447−2454.
(32) Halima, A. F.; Zhang, X.; MacFarlane, D. R. Photoelectrochemical Characterisation on Surface-Inverted Black Silicon Photocathodes by Using Platinum/Palladium Co-catalysts for Solar-to-Hydrogen Conversion. *ChemPlusChem* **2018**, *83*, 651−657.
(33) Shu, J.; Tang, D. Recent Advances in Photoelectrochemical Sensing: From Engineered Photoactive Materials to Sensing Devices and Detection Modes. *Anal. Chem.* **2020**, *92*, 363−377.
(34) Ibrahim, I.; Lim, H. N.; Abou-Zied, O. K.; Huang, N. M.; Estrela, P.; Pandikumar, A. Cadmium Sulfide Nanoparticles Decorated with Au Quantum Dots as Ultrasensitive Photoelectrochemical Sensor for Selective Detection of Copper (II) Ions. *J. Phys. Chem. C* **2016**, *120*, 22202−22214.
(35) Li, H.; Shi, Y.; Shang, H.; Wang, W.; Lu, J.; Zakharov, A. A.; Hultman, L.; Uhrberg, R. I. G.; Syväjärvi, M.; Yakimova, R.; Zhang, L.; Sun, J. Atomic-Scale Tuning of Graphene/Cubic SiC Schottky Junction for Stable Low-Bias Photoelectrochemical Solar-to-Fuel Conversion. *ACS Nano* **2020**, *14*, 4905−4915.
(36) Liu, S.; Liao, Q.; Lu, S.; Zhang, Z.; Zhang, G.; Zhang, Y. Strain Modulation in Graphene/ZnO Nanorod Film Schottky Junction for Enhanced Photosensing Performance. *Adv. Funct. Mater.* **2016**, *26*, 1347−1353.
(37) Guo, L.; Li, Z.; Marcus, K.; Navarro, S.; Liang, K.; Zhou, L.; Mani, P. D.; Florczyk, S. J.; Coffey, K. R.; Orlovskaya, N.; Sohn, Y.; Yang, Y. Periodically Patterned Au-TiO_2 Heterostructures for Photoelectrochemical Sensor. *ACS Sens.* **2017**, *2*, 621−625.
(38) Zhou, C.; Wang, S.; Zhao, Z.; Shi, Z.; Yan, S.; Zou, Z. A Facet-Dependent Schottky-Junction Electron Shuttle in a $BiVO_4${010}-Au-Cu_2O Z-Scheme Photocatalyst for Efficient Charge Separation. *Adv. Funct. Mater.* **2018**, *28*, 1801214.
(39) Xiao, J.; Han, L.; Luo, J.; Yu, S.; Jiang, H. Integration of Plasmonic Effects and Schottky Junctions into Metal-Organic Framework Composites: Steering Charge Flow for Enhanced Visible-Light Photocatalysis. *Angew. Chem., Int. Ed.* **2018**, *57*, 1103−1107.
(40) Shen, R.; Chen, W.; Peng, Q.; Lu, S.; Zheng, L.; Cao, X.; Wang, Y.; Zhu, W.; Zhang, J.; Zhuang, Z.; Chen, C.; Wang, D.; Li, Y. High-Concentration Single Atomic Pt Sites on Hollow CuS_x for Selective O_2 Reduction to H_2O_2 in Acid Solution. *Chem.* **2019**, *5*, 2099−2110.
(41) Cui, X.; Li, W.; Ryabchuk, P.; Junge, K.; Beller, M. Bridging Homogeneous and Heterogeneous Catalysis by Heterogeneous Single-Metal-Site Catalysts. *Nat. Catal.* **2018**, *1*, 385−397.
(42) Li, Y.; Kong, T.; Shen, S. Artificial Photosynthesis with Polymeric Carbon Nitride: When Meeting Metal Nanoparticles, Single Atoms, and Molecular Complexes. *Small* **2019**, *15*, 1900772.
(43) Waiskopf, N.; Ben-Shahar, Y.; Banin, U. Photocatalytic Hybrid Semiconductor-Metal Nanoparticles; from Synergistic Properties to Emerging Applications. *Adv. Mater.* **2018**, *30*, 1706697.
(44) Fang, X.; Shang, Q.; Wang, Y.; Jiao, L.; Yao, T.; Li, Y.; Zhang, Q.; Luo, Y.; Jiang, H. Single Pt Atoms Confined into a Metal-Organic Framework for Efficient Photocatalysis. *Adv. Mater.* **2018**, *30*, 1705112.
(45) Ran, J.; Jaroniec, M.; Qiao, S. Cocatalysts in Semiconductor-based Photocatalytic CO_2 Reduction: Achievements, Challenges, and Opportunities. *Adv. Mater.* **2018**, *30*, 1704649.
(46) Gao, G.; Jiao, Y.; Waclawik, E. R.; Du, A. Single Atom (Pd/Pt) Supported on Graphitic Carbon Nitride as an Efficient Photocatalyst for Visible-Light Reduction of Carbon Dioxide. *J. Am. Chem. Soc.* **2016**, *138*, 6292−6297.
(47) Huang, H.; Wang, Z.; Luo, B.; Chen, P.; Lin, T.; Xiao, M.; Wang, S.; Dai, B.; Wang, W.; Kou, J.; Lu, C.; Xu, Z.; Wang, L. Design of Twin Junction with Solid Solution Interface for Efficient Photocatalytic H_2 Production. *Nano Energy* **2020**, *69*, 104410.
(48) An, S.; Zhang, G.; Wang, T.; Zhang, W.; Li, K.; Song, C.; Miller, J. T.; Miao, S.; Wang, J.; Guo, X. High-Density Ultra-small Clusters and Single-Atom Fe Sites Embedded in Graphitic Carbon Nitride (g-C_3N_4) for Highly Efficient Catalytic Advanced Oxidation Processes. *ACS Nano* **2018**, *12*, 9441−9450.
(49) Gao, G.; Jiao, Y.; Waclawik, E. R.; Du, A. Single Atom (Pd/Pt) Supported on Graphitic Carbon Nitride as an Efficient Photocatalyst for Visible-Light Reduction of Carbon Dioxide. *J. Am. Chem. Soc.* **2016**, *138*, 6292−6297.
(50) Wu, X.; Zhang, H.; Dong, J.; Qiu, M.; Kong, J.; Zhang, Y.; Li, Y.; Xu, G.; Zhang, J.; Ye, J. Surface Step Decoration of Isolated Atom as Electron Pumping: Atomic-Level Insights into Visible-Light Hydrogen Evolution. *Nano Energy* **2018**, *45*, 109−117.
(51) Elavarthi, P.; Kumar, A. A.; Murali, G.; Reddy, D. A.; Gunasekhar, K. R. Room Temperature Ferromagnetism and White Light Emissive CdS:Cr Nanoparticles Synthesized by Chemical Co-Precipitation Method. *J. Alloys Compd.* **2016**, *656*, 510−517.
(52) Zheng, Y.; Lin, L.; Ye, X.; Guo, F.; Wang, X. Helical Graphitic Carbon Nitrides with Photocatalytic and Optical Activities. *Angew. Chem., Int. Ed.* **2014**, *53* (44), 11926−11930.
(53) Fan, G.; Zhu, H.; Du, D.; Zhang, J.; Zhu, J.; Lin, Y. Enhanced Photoelectrochemical Immunosensing Platform Based on CdSeTe@CdS:Mn Core-Shell Quantum Dots-Sensitized TiO_2 Amplified by CuS Nanocrystals Conjugated Signal Antibodies. *Anal. Chem.* **2016**, *88*, 3392−3399.
(54) Jo, W. J.; Jang, J.; Kong, K.; Kang, H. J.; Kim, J. Y.; Jun, H.; Parmar, K. P. S.; Lee, J. S. Phosphate Doping into Monoclinic $BiVO_4$ for Enhanced Photoelectrochemical Water Oxidation Activity. *Angew. Chem., Int. Ed.* **2012**, *51*, 3147−3151.
(55) Li, X.; Yu, J.; Low, J.; Fang, Y.; Xiao, J.; Chen, X. Engineering Heterogeneous Semiconductors for Solar Water Splitting. *J. Mater. Chem. A* **2015**, *3*, 2485−2534.

https://dx.doi.org/10.1021/acs.nanolett.1c00076
Nano Lett. 2021, 21, 1879−1887

(56) Tang, J.; Li, J.; Da, P.; Wang, Y.; Zheng, G. Solar-Energy-Driven Photoelectrochemical Biosensing Using TiO_2 Nanowires. *Chem. - Eur. J.* **2015**, *21*, 11288−11299.
(57) Zhu, N.; Zheng, K.; Karki, K. J.; Abdellah, M.; Zhu, Q.; Carlson, S.; Haase, D.; Zídek, K.; Ulstrup, J.; Canton, S. E.; Pullerits, T.; Chi, Q. Sandwiched Confinement of Quantum Dots in Graphene Matrix for Efficient Electron Transfer and Photocurrent Production. *Sci. Rep.* **2015**, *5*, 9860.

https://dx.doi.org/10.1021/acs.nanolett.1c00076
Nano Lett. 2021, 21, 1879−1887